

Discrete dislocation dynamics simulations of plasticity at small scales

Caizhi Zhou^{a,b}, S. Bulent Biner^b, Richard LeSar^{a,b,*}

^a *Department of Materials Science and Engineering, Iowa State University, Ames, IA 50011, USA*

^b *Ames Laboratory, Iowa State University, Ames, IA 50011, USA*

Received 10 September 2009; received in revised form 1 November 2009; accepted 1 November 2009

Available online 7 December 2009

Abstract

Discrete dislocation dynamics simulations in three dimensions have been used to examine the role of dislocation multiplication and mobility on the plasticity in small samples under uniaxial compression. To account for the effects of the free surfaces a boundary-element method, with a superposition technique, was employed. Cross-slip motion of the dislocation was also included, and found to be critical to the modeling of the dislocation behavior. To compare directly with recent experiments on micropillars, simulation samples at small volumes were created by cutting them from bulk three-dimensional simulations, leading to a range of initial dislocation structures. Application was made to single-crystal nickel samples. Comparison of the simulation results and the experiments are excellent, finding essentially identical behavior. Examination of details of the dislocation mechanism illuminates many features unique to small samples and points directly to the importance of both the surface forces and cross-slip in understanding small-scale plasticity.

© 2009 Acta Materialia Inc. Published by Elsevier Ltd. All rights reserved.

Keywords: Dislocation dynamics; Size effects; Plasticity

1. Introduction

The mechanical properties of materials change drastically when specimen dimensions are smaller than a few micrometers. Since such small structures are increasingly common in modern technologies, there is an emergent need to understand the critical roles of elasticity, plasticity and fracture in small structures. Small-scale structures also offer opportunities for direct comparison between modeling and experiment at previously inaccessible scales. The experiments provide data for validation of models, and the models provide a path for new, physically based understanding and prediction of materials behavior. Mechanical tests at nanometer or micrometer scales are difficult to perform, but they provide guidance to develop new technologies and new theories of plasticity. Experimental studies on the mechanical behavior of small structures are not new; the first work on thin

metal whiskers (with diameters of $\sim 100\ \mu\text{m}$) was performed more than 50 years ago [1]. The past few years, however, have seen a major leap forward in the experimental study of small samples. We focus here on studies of metals, highlighting examples of previous work.

Uchic et al. recently pioneered the study of size effects in compression of $1\ \mu\text{m}$ diameter metal samples [2–6]. Cylindrical pillars with varying radii were machined with a focused-ion beam (FIB) from single-crystal bulk samples and compressed by a blunted nanoindenter. This pioneering work spurred similar activities from several groups, with studies on a range of sample sizes, from sub-micron to many-micron [7–11]. Studies on face-centered cubic (fcc) metals show that flow stress increases as system size decreases, with the onset of deviation from bulk behavior varying somewhat from material to material. The increased flow stress is accompanied by extremely large strain hardening at small to moderate strains, with small samples showing higher strain-hardening rates [3,12,13]. Indeed, very small samples can achieve extremely high flow stresses, e.g. a cylinder with a diameter of about $0.2\ \mu\text{m}$ in nickel can sustain a stress of up to 2 GPa [12]. This general result that yield stress increases as system

* Corresponding author. Address: Department of Materials Science and Engineering, Iowa State University, 2220 Hoover Hall, Ames, IA 50011, USA.

E-mail address: lesar@iastate.edu (R. LeSar).

size decreases is also found in other tests on fcc materials, including a study using atomic force microscopy (AFM) to bend gold nanowires [14] and also in polycrystalline membranes of copper, gold and aluminum in pure tension [15]. Probably the most accepted explanation of these size effects is the “dislocation starvation” model [7,8], in which dislocations are drawn to free surfaces by strong image forces and exit the crystal. Recent work on body-centered cubic (bcc) molybdenum alloys showed that both the initial yield stress and size-dependent hardening rate are strongly dependent on initial dislocation density [16], an issue not well studied in the fcc metals.

Key to an understanding of these size effects is a characterization of the internal structure of microscale samples. Some work has been done with transmission electron microscopy (TEM), but there are limitations of the thickness of samples that can be studied with TEM—thin foils must be cut from the samples and the results thus depend on the plane of the foils as well as the size and orientation of the microstructures. Results from these studies are reasonably consistent, however, showing a small net increase in dislocation density after the initial loading [8,17]. A recent study using a novel in situ TEM micropillar method showed evidence of “mechanical annealing”, a sudden drop in dislocation density upon initial loading and a subsequent small increase in density with further compression [18]. Micro X-ray diffraction (XRD) studies [19–21] of lattice rotations in these systems indicate approximately the same dislocation contents as TEM measurements [22–25]. Overall, it is clear that dislocation densities and activities are greatly affected by system size, but the connection between size-dependent strengthening and dislocation activity is not yet clearly established.

The recent increase in experimental deformation data in confined geometries has been accompanied by a similar focus on the use of modeling and simulation on small samples. Discrete dislocation simulations, in which the dislocations are the simulated entities, offer a way to extend length scales beyond those of atomistic simulations [26–30]. Simply put, dislocation-based simulations: (i) represent the dislocation line in some convenient way; (ii) determine either the forces or interaction energies between dislocations; and (iii) calculate the structures and response of the dislocations to external stresses. These simulations are useful for mapping out the underlying mechanisms by providing “data” not available experimentally on, for example, dislocation ordering, evolution of large-scale dislocation structures (walls, cells, pile ups), dynamics (avalanches and instabilities), etc. For the micron-scale systems described above, recent dislocation dynamics (DD) simulations have provided important insights into the mechanisms that determine the size-affected mechanical response.

The first attempts to explain the micropillar results using DD assumed two-dimensional (2D) models [31–33]. These assumptions inherent in such simplified models limit their applicability owing to the inherently 3D nature of plasticity. Recent 3D simulations by a number of groups employing a variety of approximations and models have shed

some light on the fundamental processes. The agreement between calculation and experiment is, in general, reasonably satisfactory [34–38]. All calculations show bulk-like behavior for larger system sizes, dominated by forest-obstacle hardening, and a “starvation” regime when the sampled volumes fall below a length scale seemingly set by the correlation length of the dislocation forest [6].

In real crystals, dislocation structures are much more complicated than the set of isolated Frank–Read (FR) sources that were used as the initial configuration in most previous DD simulations [31–38]. Recently, Tang et al. [39] used artificial jogged dislocations as starting dislocation populations for their simulations neglecting the boundary conditions and cross-slip, and stated that source shut-down causes the staircase behavior observed in experiments. Motz et al. [40] used the dislocation structures relaxed from closed dislocation loops as the initial input for 3D DD simulations. Thus, there were no initial pinning points. They found a pronounced size effect for the flow stress depending on the initial configuration and the specimen size. In the study reported here, an experimental-like initial dislocation structure cut from larger deformed samples has been introduced into 3D DD simulations, which contains all the dislocation sources considered in all previous DD simulations, such as FR sources, jogged dislocations, surface dislocations and spiral (single-armed) sources. Thus the simulations could directly examine the role of evolution of microstructures on size effects.

The goal of this work was to model the experiment as closely as possible. In addition to creating initial conditions that best mimic experiment, the simulations discussed here also include two effects not generally included in previous simulations: surface forces and cross-slip. Surface forces were included through the use of the boundary-element method [38]. Cross-slip was modeled with a stochastic method and was found to play a critical role in dislocation behavior. Finally, the effects of loading direction were also studied.

While progress has been made both experimentally and theoretically to understand small-scale plasticity, many important questions remain. Despite the relatively few dislocations in these small samples, we still have a limited understanding of the correlation between dislocation motion and the mechanical response. Specifically, we need to better identify what critical events (i.e. dislocation multiplication, cross-slip, storage, nucleation, junction and dipole formation, pinning, etc.) determine the deformation response and how these change from bulk behavior as the system decreases in size. Indeed, a fundamental question is how we correlate and improve our current knowledge of bulk plasticity with the knowledge gained from the direct observations of small-scale plasticity. Our simulations offer some new insight into these questions.

2. Simulation procedures

The 3D DD simulation framework described in Refs. [27,38] has been used in our study to simulate the mechan-

ical behavior of Ni single crystals under uniform compression. In this method, an explicit numerical scheme is used to obtain the evolution of the dislocation configurations at each step by tracking the motion of a discrete mesh of nodes along each dislocation line. The Peach–Koehler (PK) equation is used to determine the force per unit length acting locally on the dislocations:

$$\mathbf{F}_{\text{PK}} = ((\sigma_{\text{app}} + \sigma_{\text{int}} + \sigma_{\text{img}}) \cdot \mathbf{b}) \times \mathbf{t} + \mathbf{F}_{\text{self}}, \quad (1)$$

where σ_{app} is the uniaxial stress tensor which is applied homogeneously in the sample, σ_{int} is the stress tensor from the other dislocation segments, σ_{img} the image stress tensor taking into account free surfaces, \mathbf{b} is the Burgers vector of the dislocation, \mathbf{t} is the line direction of the segment and \mathbf{F}_{self} is the force arising from the segment itself and from immediately adjacent segments, which can be calculated by a line tension approximation. Once the PK forces on dislocation segments have been obtained, we solve the equations of motion to determine the rate of change of dislocation structure. For the simulations in this work, the materials properties of nickel are used: shear modulus $\mu = 76$ GPa, Poisson's ratio $\nu = 0.31$ and lattice constant $a = 0.35$ nm. The dislocation mobility is taken to be $10^{-4} \text{ Pa}^{-1} \text{ s}^{-1}$ in the calculations [51].

In finite-volume problems, it is necessary to include both the solution for dislocations in an infinite medium and the complementary elastic solution that satisfies equilibrium at external and internal boundaries. According to the superposition method of Ref. [41], the total displacement and stress fields are given as

$$u_{ij} = \tilde{u}_{ij} + \hat{u}_{ij} \text{ and } \sigma_{ij} = \tilde{\sigma}_{ij} + \hat{\sigma}_{ij}, \quad (2)$$

where \tilde{u}_{ij} and $\tilde{\sigma}_{ij}$ are the displacement and stress fields in an infinite medium from all dislocations, while \hat{u}_{ij} and $\hat{\sigma}_{ij}$ are the image fields that enforce the boundary conditions. To evaluate image fields, a boundary-element method (BEM) has been introduced into our DD simulations and performed as follows. First, the elastic stress field in an infinite medium resulting from all dislocations is evaluated. Then tractions at the surfaces of the finite crystal owing to the dislocation stress field are determined, reversed and placed on the surface as traction boundary conditions. These traction boundary conditions, as well as any other imposed constraints, are employed in the BEM to calculate all unknown surface tractions and displacements. Finally, the image stress field is calculated and the result is superimposed as indicated in Eq. (2). More details on this procedure can be found elsewhere [38,42].

Cross-slip, in which screw dislocations leave their habit planes and propagate to another glide plane [43,44], plays a key role in macroscopic plastic deformation of fcc materials. However, questions of how cross-slip operates and its importance at the micron and sub-micron scales are still under debate. In this study, we adopt a sophisticated cross-slip model developed by Kubin and coworkers [28,45] that is based on the Friedel–Escaig mechanism of thermally activated cross-slip [46,47]. In this model, the

probability of cross-slip of a screw segment with length L in the discrete time step is determined by an activation energy $V_{\text{act}}(|\tau| - \tau_{\text{III}})$ and the resolved shear stress on the cross-slip plane τ :

$$P = \beta \frac{L}{L_0} \frac{\delta t}{\delta t_0} \exp \left[-\frac{V_{\text{act}}}{kT} (|\tau| - \tau_{\text{III}}) \right], \quad (3)$$

where β is a normalization constant, k is the Boltzmann constant, T is set to room temperature, V_{act} is the activation volume and τ_{III} is the stress at which stage 3 hardening starts. In nickel, V_{act} is equal to $420b^3$ with b the magnitude of the Burgers vector [48], $\tau_{\text{III}} = 55$ MPa [49], and $L_0 = 1 \mu\text{m}$ and $\delta t_0 = 1$ s are reference values for the length of the cross-slipping segment and for the time step. Eq. (3) describes the thermal activation of cross-slip, expressed in terms of a probability function. A stochastic (Monte Carlo) method is used to determine if cross-slip is activated for a screw dislocation segment. At each time step, the probabilities for cross-slip of all screw segments are calculated using Eq. (3). For each screw segment, the probability P is compared with a randomly generated number N between 0 and 1. If the calculated P is larger than N , cross-slip is activated; otherwise, the cross-slip is disregarded [50,51].

Our goal is to mimic the experimental conditions as well as possible. To that end, we start by creating a “bulk” sample, from which we will “cut” a set of cylindrical samples. To model the bulk, we assume a cubic cell with periodic boundary conditions and a size $3 \times 3 \times 3 \mu\text{m}^3$ containing a set of FR sources with an initial density equal to $2.0 \times 10^{12} \text{ m}^{-2}$. The FR sources (straight dislocation segments pinned at both ends) were randomly set on all 12 $\langle 011 \rangle \{111\}$ slip systems with random lengths as shown in Fig. 1a. After compression in the $[111]$ direction to a plastic strain of 0.1%, the distribution of dislocations evolves to the structure shown Fig. 1b with a dislocation density of about $2.5 \times 10^{13} \text{ m}^{-2}$. The cubic sample was unloaded (i.e. relaxed) and cylinders of various sizes (representing micropillars) were cut out of the bulk sample. The diameters D of the micropillars were $D = 1.0, 0.75$ and $0.5 \mu\text{m}$, and the aspect ratio was set to $D:H = 1:2$, where H denotes the height of micropillars. Subsequently, the deformed dislocation microstructures were relaxed only under the influence of image and interaction forces as shown in Fig. 2a and b. Most of the micropillars were cut along the $[001]$ direction, except for three samples along the $[269]$ direction with $D = 1.0 \mu\text{m}$. This procedure delivers what we assume to be realistic initial dislocation structures that include internal FR sources of different sizes, single-ended sources (spiral sources with one end pinned inside the cell and the other at the surface), surface dislocations (both ends at surface) and dislocation reactions, such as junctions. The dislocation densities after relaxation were all in the range of $1.0\text{--}2.0 \times 10^{13} \text{ m}^{-2}$ and were consistent with conditions observed in experiments [52].

We simulated the experimental loading conditions of Dimiduk and coworkers [2–5,52] in our computations, in which a mixture of constant displacement rate and creep-

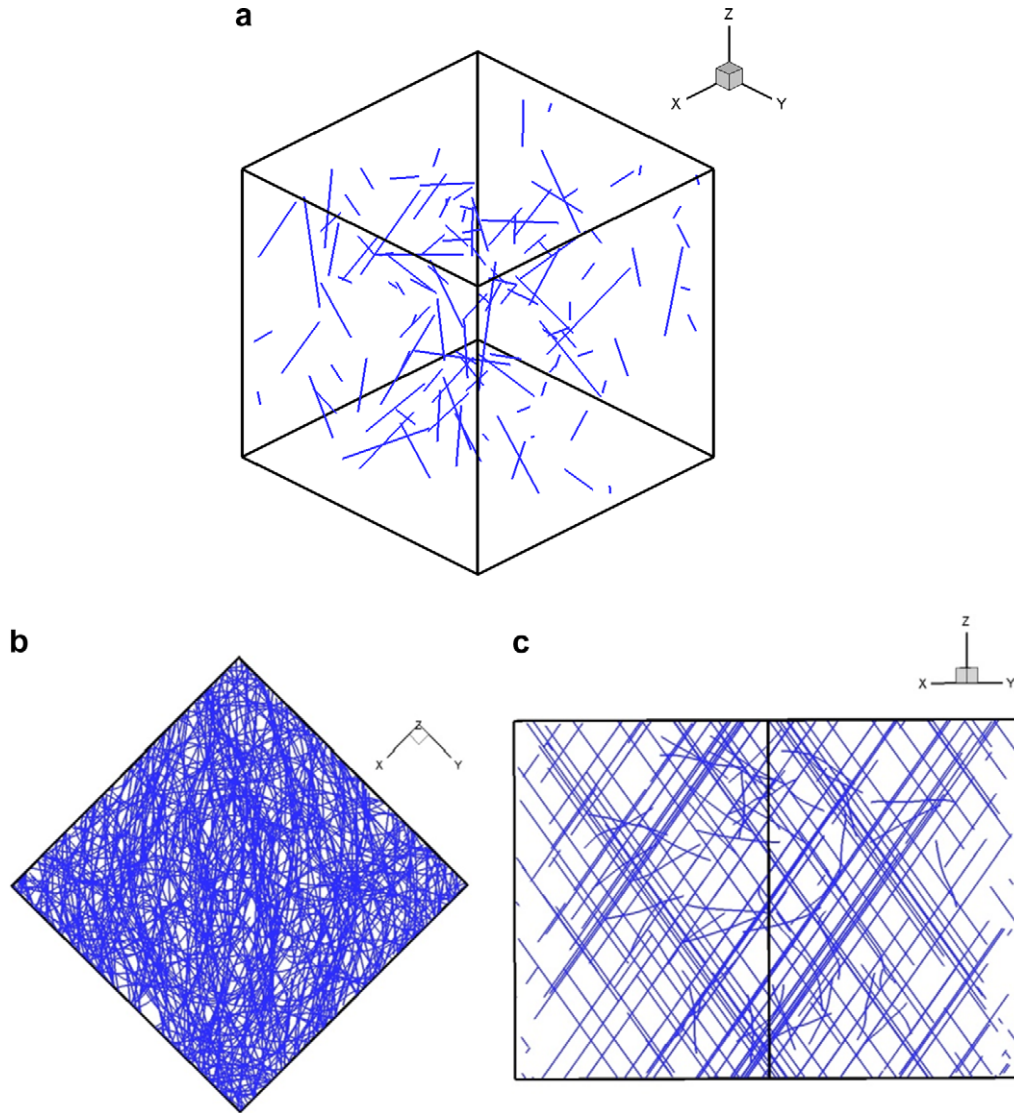


Fig. 1. Dislocation structures in $3 \times 3 \times 3 \mu\text{m}^3$ cube sample. (a) Initial dislocation structure in $[1\ 1\ 1]$ view; (b) deformed structure in $[0\ 0\ 1]$ view; (c) deformed structure in $[1\ 1\ 0]$ view.

like loading conditions were employed; the applied stress was discretely increased by a small fixed value ($\delta\sigma$) every time the plastic strain rate approached zero. When the plastic strain rate was smaller than the applied rate, the applied load was increased by 2 MPa, i.e. $\delta\sigma = 2 \text{ MPa}$, for $\dot{\epsilon}^p < \dot{\epsilon}$, while the applied stress was kept constant when the plastic strain rate was equal to or higher than that of the applied rate, i.e. $\delta\sigma = 0$, for $\dot{\epsilon}^p \geq \dot{\epsilon}$.

The plastic strain rate $\dot{\epsilon}^p$ is computed from the motion of the dislocations as follows:

$$\dot{\epsilon}^p = \frac{1}{2V} \sum_{i=1}^{N_{tot}} l_i^\alpha v_i^\alpha (\mathbf{b}_i \otimes \mathbf{n}^\alpha + \mathbf{n}^\alpha \otimes \mathbf{b}_i), \quad (4)$$

where V is the volume of the simulated crystal, N_{tot} is the total number of dislocation segments, l_i^α is the length of dislocation segment i moving on the slip plane α , and v_i^α is the corresponding moving velocity of the segment i . \mathbf{b}_i and \mathbf{n}^α

are the Burgers vector of dislocation segment i and the normal of slip plane α , respectively.

In all simulations, compression loading in the $[0\ 0\ 1]$ direction was performed under a constant strain rate of 200 s^{-1} . To identify the effects of strain rate, several simulations were performed with strain rates as low as 50 s^{-1} . The results from those simulations did not show any significant difference from those seen at 200 s^{-1} . We found that a strain rate of 200 s^{-1} is computationally efficient with negligible effect on the results while also being lower than the strain rates used in other, similar, simulations [34,37,40].

To investigate the effects of loading direction, as well as to make a direct comparison with the experimental results of Dimiduk et al. [3], we also prepared three $1.0 \mu\text{m}$ samples oriented in the $[2\ 6\ 9]$ direction. We see distinct differences in the two typical initial dislocation structures from the $[0\ 0\ 1]$ and $[2\ 6\ 9]$ samples as shown in Fig. 2c and d, respectively. Since the stress was then applied along the

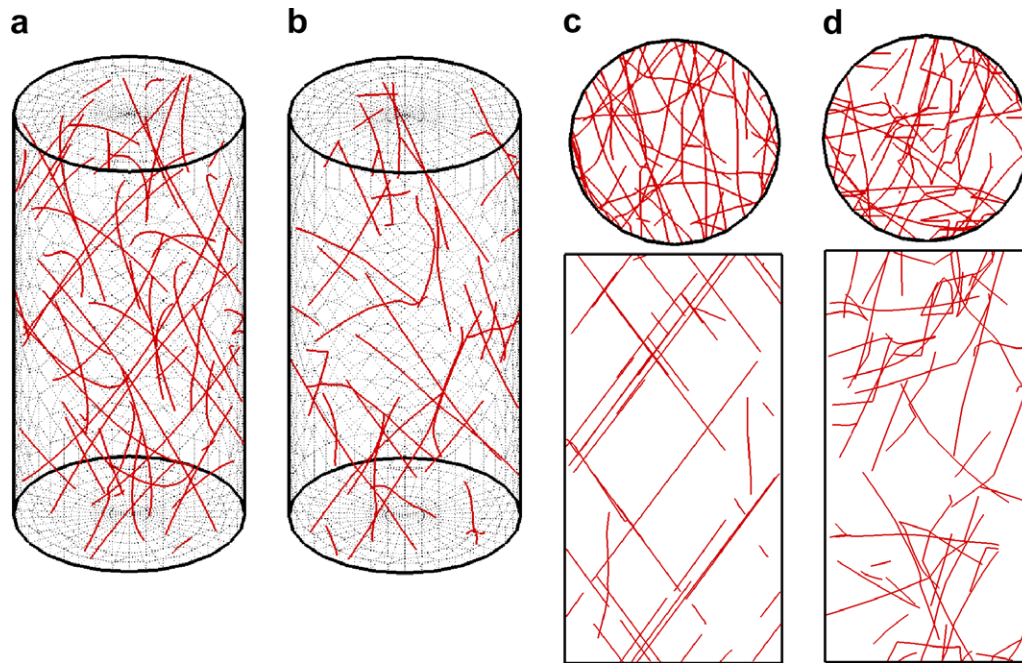


Fig. 2. Dislocation structures in cut samples with $D = 1.0 \mu\text{m}$ (dotted lines are BEM meshes). (a) Cutting from $[001]$ before relaxation with density $= 2.7 \times 10^{13} \text{ m}^{-2}$, view in $[111]$ direction; (b) cutting from $[001]$ after relaxation with density $= 1.9 \times 10^{13} \text{ m}^{-2}$, view in $[111]$ direction; (c) cutting from $[001]$ direction with density $= 1.9 \times 10^{13} \text{ m}^{-2}$ upper in $[001]$ view, lower in $[110]$ view; (d) cutting from $[269]$ direction with density $= 2.0 \times 10^{13} \text{ m}^{-2}$ upper in $[001]$ view, lower in $[110]$ view.

$[001]$ axis, the simulations correspond to a single-slip direction for samples cut from the $[269]$ direction and along a multi-slip direction for samples cut along the $[001]$ direction. For the single-slip case, only the $1/2[101](\bar{1}11)$ slip dislocation system has the maximum Schmid factor (equal to 0.48). For the multi-slip case, eight slip systems are active, each with the same Schmid factor of 0.41, whereas the other four slip systems have zero Schmid factors and are inactive.

3. Results and discussion

3.1. Effect of loading direction

The stress–strain behavior for all simulations based on $1.0 \mu\text{m}$ samples is shown in Fig. 3a, while the equivalent experimental results for single-crystal nickel are shown in Fig. 3b. Comparing Fig. 3a and b, we see that the flow stress of the multi-slip simulations (from the $[001]$ samples) and the single-slip simulations (from the $[269]$ samples) are both similar to each other and agree well with the experimental results, which employed loading along the $[269]$ single-slip direction. In our simulations, only one, or at most a few, mobile dislocations determined the strength at small volumes. Thus, multiple-slip simulations and single-slip simulations exhibited similar results. The agreement between the results for single-slip and multi-slip loading is not surprising in light of recent results. Norfleet et al. [52] recently examined cut foils from deformed pillars and found that for samples $<20 \mu\text{m}$ in diameter, multiple-

slip systems are always active regardless of the loading direction. In addition, a recent theoretical study by Ng et al. concluded that Schmid's law, which states that plastic flow will occur on the slip system with the largest Schmid factor, no longer holds for microcrystal deformation, because of the increase of the probability to activate sources with low Schmid factors in small samples, as the overall number of dislocation sources decreases with the sample diameter [53]. Thus, both experiment and modeling indicate that single-slip and multiple-slip deformation should be similar in these small samples.

Recent 3D DD simulations that were based on an initial dislocation structure within the cylinder consisting of only internal FR sources showed linear elastic loading up to the yield point [34,35,37]. In contrast to those results, our simulations showed a large amount of "microplasticity" at low loads (shown in Fig. 3a), in agreement with the experimental results (shown in Fig. 3b). This early-stage plasticity is often the result of essentially free dislocations being driven out of the system. These dislocations could either be weakly entangled or pre-existing at the surface. Movie A in [Supplementary material](#) of this paper illustrates one example of how a dislocation junction unzipped and then was driven out of the sample as load was increased. The presence of such dislocations can be explained as follows. After cutting the cylinders out of the bulk system, we relax the dislocation positions. While some of surface dislocations escape to the surface owing to the large image forces, many dislocations can be trapped by dislocation reactions, such as junctions, or be near the center of the sample where

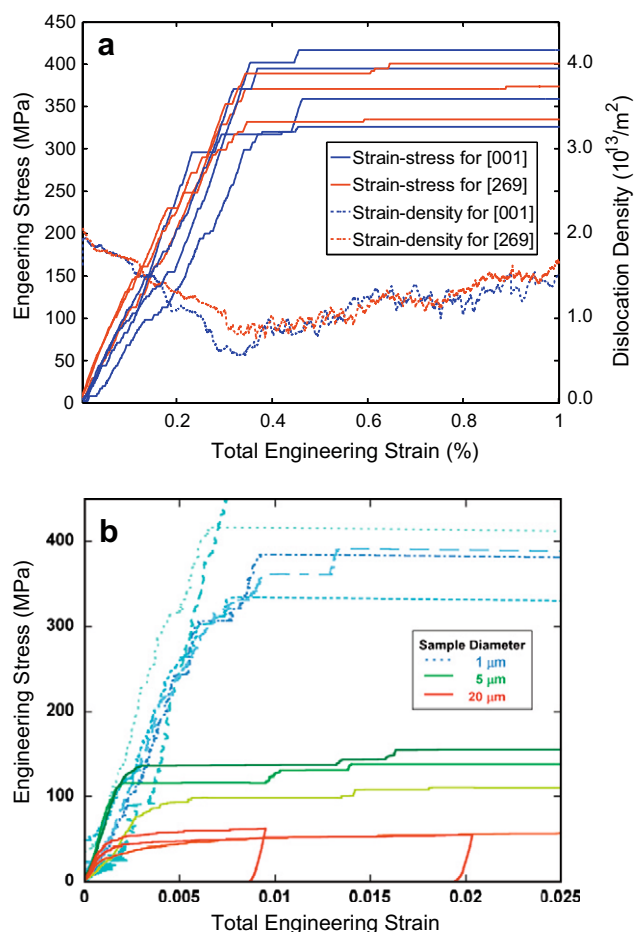


Fig. 3. Comparison of stress–strain curves of simulation and experiment. (a) Stress–strain and typical density–strain curves obtained from simulation with $D = 1.0 \mu\text{m}$. (b) Stress–strain curves obtained from experiment [3].

the image forces are insufficient to cause any significant movement [54]. In experiments, a large number of surface dislocations of different sizes might also exist in the micropillars. These dislocations may be generated by the act of the cutting, but could also arise from defects caused by preparation procedures themselves, such as FIB milling [16].

As the loading is increased, the motion of free dislocations is gradually activated. The dislocations then sweep quickly across the slip plane, exiting the micropillar, leading to a rapid reduction in dislocation content referred to as “dislocation starvation”. The easy movement of these free dislocations leads to a plastic strain rate that approaches the applied strain rate, which causes the applied stress increment to approach zero, as mentioned in the discussion of the loading scheme. Thus, we see an initial small strain burst on the stress–strain curves. The amount of plastic strain in our simulations is smaller than that observed in experiments, which likely arises from two possibilities. Experimental samples are all processed by FIB milling, leading to many surface defects. It has been suggested that these surface defects can generate plastic

strain under loading [55]. Also, the 200 s^{-1} strain rate in our simulation is four orders of magnitude larger than those in the experiments, which have a creep-like loading and thus can carry more deformation at low loads.

Owing to the escape of free dislocations, the dislocation density in all samples will decrease in the early stages as reflected by the density–strain curves in Fig. 3a. In previous 3D DD simulations [34,35,37], only permanent internal FR sources were used as the initial configuration. Thus, the dislocation density could not decrease even with the intermittent presence of mobile density-starved states. In our simulation procedure, in small pillars, only a few surface dislocations, a few jogged dislocations and no internal pinned points could be found in inside the cylinder. Under the combination of high image forces and increased applied loading (and no cross-slip, as discussed below), all pre-existing dislocations can be quickly driven out of the pillar, which supports the “dislocation starvation” model in small samples. Recently, Shan et al. [18] directly observed that pre-existing dislocations could be driven out of the pillar with the entire length of the pillar being left almost dislocation free for pillars with diameter less than 130 nm. This phenomenon, which was called “mechanical annealing”, directly supports the ideas behind the “dislocation starvation” model in smaller samples. However, for pillars larger than 300 nm, pre-existing dislocations could not be completely driven from the cylinder, which indicates that permanent pinning points exist in those micropillars and that the dislocation density will eventually increase following the initial “mechanical annealing”. These experimental results agree well with what is observed in our simulations as plotted in Fig. 3a. The dislocation density increase following “mechanical annealing” was caused by the activation of dislocation sources and dislocation multiplication with the increasing load arising from cross-slip, as is described in the next section.

3.2. Cross-slip

To investigate the influence of cross-slip on the mechanical response and evolution of the dislocation microstructure, an additional sample with $D = 1.0 \mu\text{m}$ was cut from the undeformed cube shown in Fig. 1a. Thus, only FR and spiral sources were initially present, with an initial density of $1.8 \times 10^{12} \text{ m}^{-2}$ in the sample. This sample was then put under load both with and without cross-slip enabled. In Fig. 4 we show the comparison of microstructures and the stress and density evolution for these two cases. It is clear that the sample with cross-slip is softer than that without cross-slip, likely because cross-slip leads to more sources and thus greatly increased dislocation density, as shown in Fig. 4d. We note that the cross-slip started at the onset of plastic flow.

Fig. 5 shows a series of snapshots that illustrate how cross-slip activates secondary slip systems and enables oppositely signed screw dislocations on different planes to annihilate each other. The two red dislocations $L1$ and

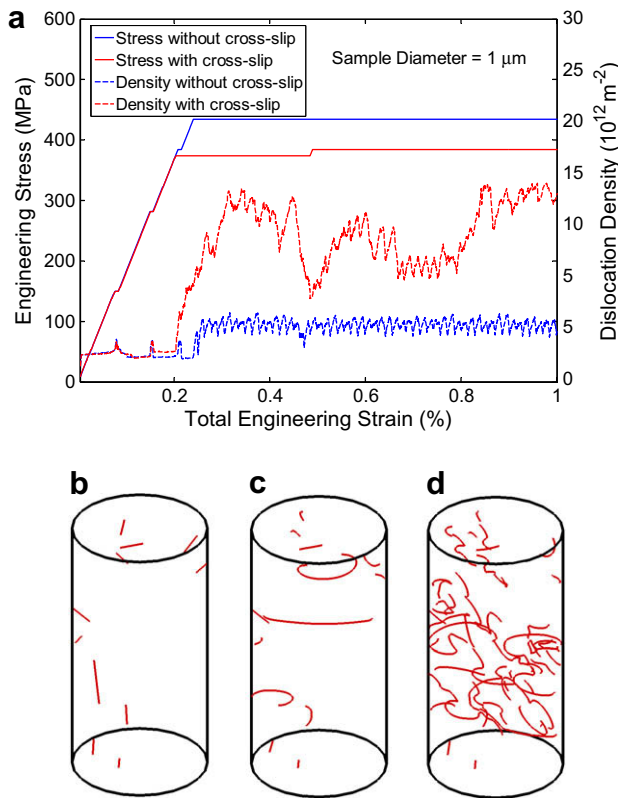


Fig. 4. Comparison of the stress and density evolution for 1.0 μm sample with and without cross-slip: (a) stress and density curves, (b) initial dislocation structure, (c) dislocation structure without cross-slip at 1% strain and (d) dislocation structure with cross-slip at 1% strain.

$L2$ have the same slip system $1/2[101](\bar{1}\bar{1}1)$ on parallel glide planes but opposite initial orientations. Hence, there is an attractive force between the two dislocations that makes the screw segment $J1$ of dislocation $L1$ cross-slip on the plane $(\bar{1}\bar{1}1)$. $J1$ continues bowing out under the attractive force until its leading segments undergo a collinear reaction with the original dislocation $L2$ (they have the same Burgers vector and opposite line orientation). In Fig. 5c, we can see that two superjogs were left after the collinear reaction. Under the external stress field, the two arms of superjogs moved on their slip planes and formed a prismatic loop, as shown in Fig. 5d. The prismatic loops are quite stable and can move only along the cylinder axis. Since this motion is difficult, the prismatic loops are fixed at the location at which the cross-slip occurred. They can then trap mobile dislocations, forming a dislocation forest as shown in Fig. 5d, which has a strong influence on the subsequent plastic flow in small volumes.

In Fig. 6 we show the variation of dislocation density as a function of sample size and total strain. For all sizes studied in this study, the dislocation density initially dropped (“mechanical annealing”), followed by a steady increase (hardening). The dislocation density is reasonably insensitive to system size, with the point at which the density begins to rise occurring at approximately the same strain (approximately 0.4%) for all samples. Below we shall discuss the behavior of the dislocation density in more detail.

The basic behavior of the hardening arises from the cross-slip mechanisms shown in Fig. 7. At the beginning of the deformation, only a few dislocation sources are available after most of the free dislocations have been driven out of the sample, as shown in Fig. 7a and described above. Under increasing load, a spiral source $K1$ with Burgers vector $1/2[\bar{1}01]$ was activated and moved in its slip plane (111) in Fig. 7b. Screw segment $C1$ then cross-slipped on the slip plane $(\bar{1}\bar{1}1)$ with the same Burgers vector, forming two joint corners $p1$ and $p2$, both of which then moved along the intersection line between the original slip plane and the cross-slip plane (Fig. 7c, discussed in detail below). After extending on the slip plane under load, the original source $K1$ was truncated by the free surface and then stopped moving in Fig. 7d. However, the cross-slipped part $C1$ and non-cross-slipped parts $K2$ and $K3$ truncated from $K1$ propagated smoothly until they encountered the free surface. In Fig. 7e, the screw part $C2$ on $C1$ cross-slipped back to the original slip plane (111) (double cross-slip), a mechanism that generates considerable plastic strain in the deformation of bulk materials. Meanwhile, $K2$ and $K3$ behaved similarly to FR sources in the bulk, in that they annihilated each other and generated new dislocations $K4$ and $K5$.

The major difference between multiplication processes observed in small volumes and those in the bulk is that the new dislocations, such as $K5$, escape to the surface under the influence of image forces. In small volumes, it appears that the surface always confines dislocation propagation, having a potent hardening effect as sample size decreases because of the shortening of the dislocation sources. In our simulations, this “source-truncation” [56] effect is reflected in Fig. 7d, in which the original spiral source $K1$ was pinned after being truncated by the surface. From Fig. 7e–h, the two joint corners $p1$ and $p2$ formed a new dynamic FR source that continuously generated dislocations on two different slip planes, leading to the constant-stress avalanches reflected on the stress–strain curves. However, this dynamic FR source is not as stable as regular FR sources having permanent pinning points, since the two endpoints of a dynamic FR source might move out of the sample surface, thereby releasing the dynamic source. The stability of these sources increases with the increased sample size, affecting their contribution to the accumulated plastic strain of the sample and the increase of dislocation density.

3.3. Exhaustion hardening

In our simulations, superjogs and dynamic spiral sources, as illustrated in Fig. 8a and b, were always formed by cross-slip or collinear reactions [57] combined with the truncation by free surfaces. The superjog AO_1O_2B with two ends A and B at the surface in Fig. 8a is similar to jogs artificially generated in Ref. [39], except that in our simulations they were formed naturally. One difference in behavior between [39] and the present results is that the middle

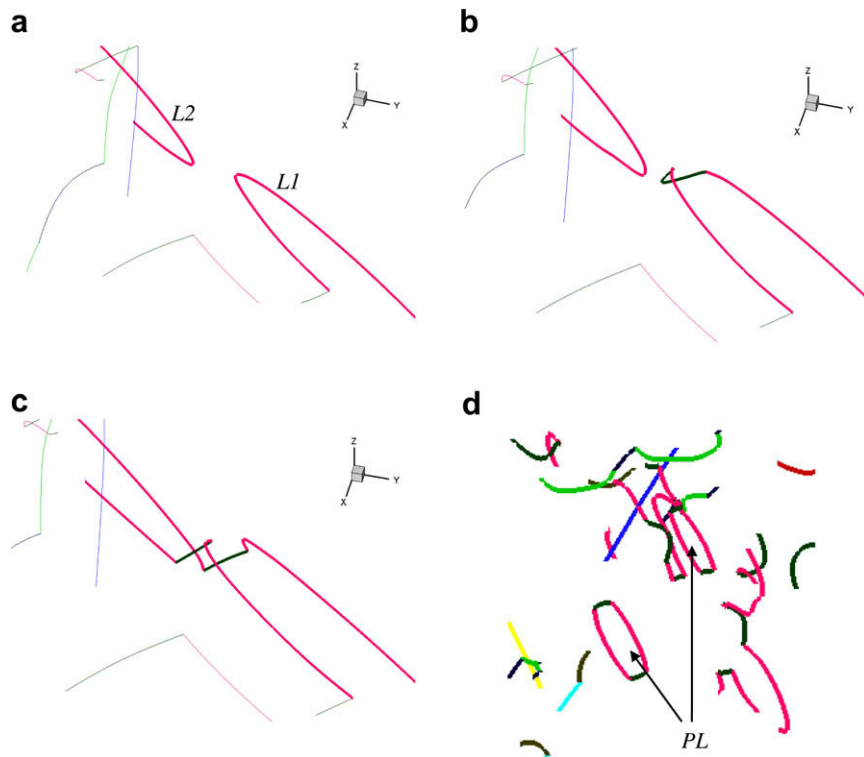


Fig. 5. Plot of cross-slip on parallel dislocations and formation of prismatic loop (PL): pink line with $1/2[101](\bar{1}11)$ and green line with $1/2[101](\bar{1}\bar{1}1)$. (a) Two parallel dislocations slip on its own planes; (b) one dislocation cross-slip under the attractive force; (c) collinear reaction of the leading segments forming two superjogs; (d) prismatic loops. (For interpretation of the references to colour in this figure legend, the reader is referred to the web version of this article.)

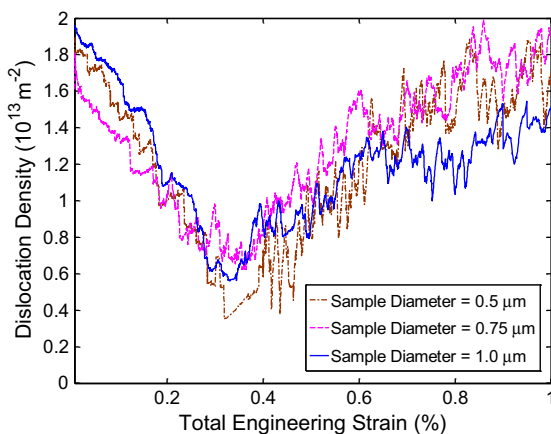


Fig. 6. Evolution of dislocation density with total strain.

segment O_1O_2 bowed out under sufficient force in this study. Under loading, the two dislocation arms, AO_1 and BO_2 operated independently around the jog corners O_1 and O_2 , producing continuous plastic flow. When O_1O_2 is short enough, the superjog AO_1O_2B formed an intermediate jog, as the dislocations arms AO_1 and BO_2 interacted like dislocation dipoles and could not pass by one another except at a high stress [58]. Once the resolved shear stress on segment O_1O_2 is large enough, it bowed out like an FR source. If it was truncated by the free surface, this superjog AO_1O_2B transformed into two dynamic spiral

sources, e.g. AOB in Fig. 8b. These two dislocation arms of these dynamic sources were rotated around the jog corners O , again producing continuous plastic flow. This type of dynamic spiral source was not seen in Ref. [39], since the middle segment of superjog was sessile and cross-slip was not considered in their simulation. As illustrated in Fig. 8, the joint points, O_1 and O_2 in superjog AO_1O_2B , and O in the dynamic spiral sources AOB , moved along the intersection line of the two intersected slip planes. When these joint points moved close to the free surface with its attractive image forces, they escaped and the dynamic spiral sources or superjogs ceased to operate. Movie B in Supplementary material gives one example of flow intermittency as the moving dynamic spiral source escaped from free surface. The dynamic spiral source has two arms on different slip planes as shown in Fig. 8b. With increasing load, they could operate independently on their own slip planes, and the joint point could move along the intersection line of the two slip planes. The stability of this dynamic source depends on the exact position of the jog corner and the sample diameter. For this source, after operating several times and generating a certain amount of plastic strain, it gradually escaped from the free surface and ceased to operate. Since there were no other operating sources, to sustain the applied strain rate required that the elastic strain (linearly related to the applied stress) increased until another source could be activated. During this period, the fraction of plastic strain in the total strain

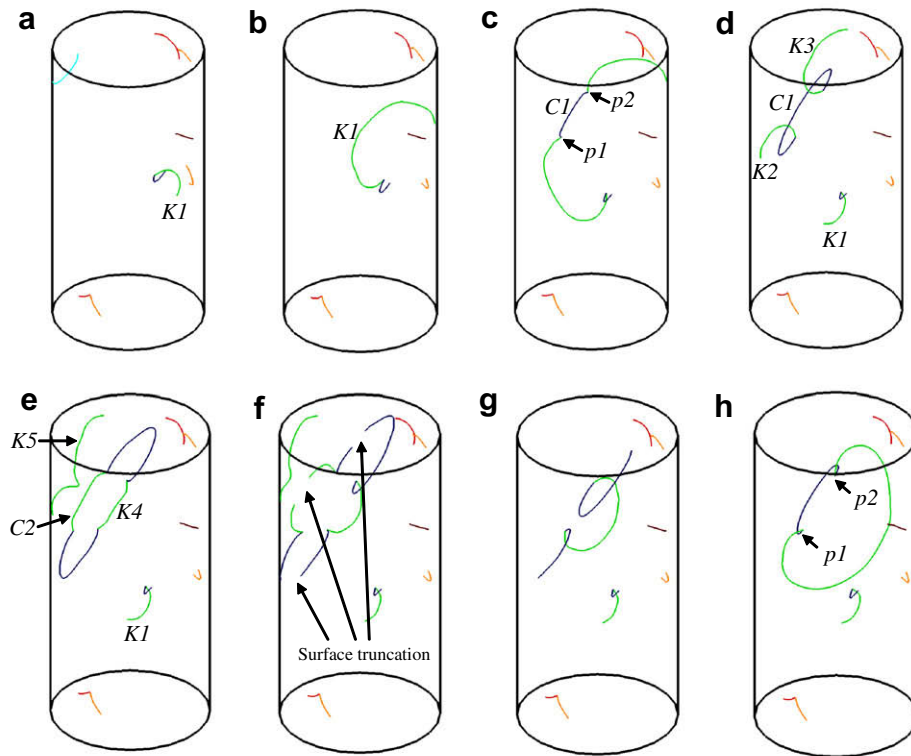


Fig. 7. Plot of cross-slip forming dynamic FR source: green line with $1/2[\bar{1}01](111)$ and blue line with $1/2[\bar{1}01](1\bar{1}1)$, see details in text.

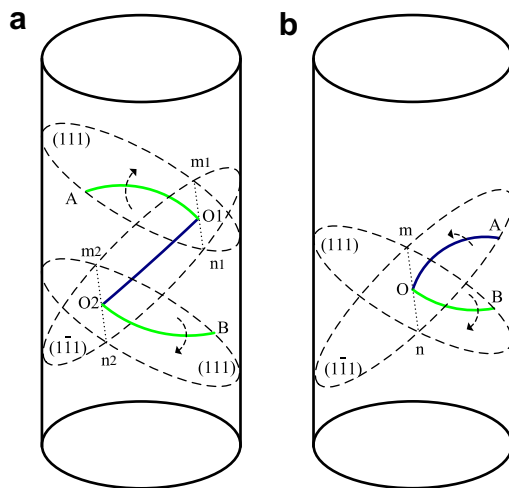


Fig. 8. Configuration of superjog and dynamic spiral source: green line with $1/2[\bar{1}01](111)$ and blue line with $1/2[\bar{1}01](1\bar{1}1)$. (For interpretation of the references to colour in this figure legend, the reader is referred to the web version of this article.)

approached zero (no operating sources) and the strain-hardening part was thus essentially elastic. This dislocation-starved condition (the shutting off of available dislocation sources) is called “exhaustion hardening”, and is found both in experiments and simulations [18,40]. After the applied stress increased to a sufficiently high level, new sources were activated, generating plastic strain. Again, to keep the same overall strain rate, the elastic strain (applied stress) stopped increasing, leading to a plateau

in the stress–strain curve corresponding to continuous operation of this new source. This type of dynamic source showed considerable variability in behavior. In some cases, the sources just operated several times and then escaped to the surface. While in others they were stable and operated numerous times, existing as long as the simulations were run. Thus, the degree of “exhaustion hardening” caused by the destruction of dynamic sources cannot be predicted a priori and requires knowing the details of the internal dislocation structures. We can say, however, that the frequency of this mechanism is much higher in smaller samples, in which the dynamic sources are more easily destroyed at the surface and then regenerated.

The size-dependent exhaustion processes also affect the usual forest-hardening processes of junction formation and dipole interactions, resulting in the shutting off of already scarce dislocation sources. Fig. 9 shows two typical cases of junction formation and collinear reaction, which leads to intermittent plastic flow. This mechanism has been observed previously by Rao and coworkers [35]. In Fig. 9a, the single-ended spiral source $S1$ sweeps in its slip plane until it meets the FR source $S2$. As $S1$ moves close to $S2$, a glissile junction was formed, locking the dislocations as shown in Fig. 9b and c. When the applied stress is increased to a critical value, the glissile junction unzipped and the spiral source $S1$ cyclically rotated around the pinning point and created continual plastic strain for the sample in Fig. 9d. In contrast to glissile junction, the collinear reaction formed by two mobile spiral sources in Fig. 9e–h

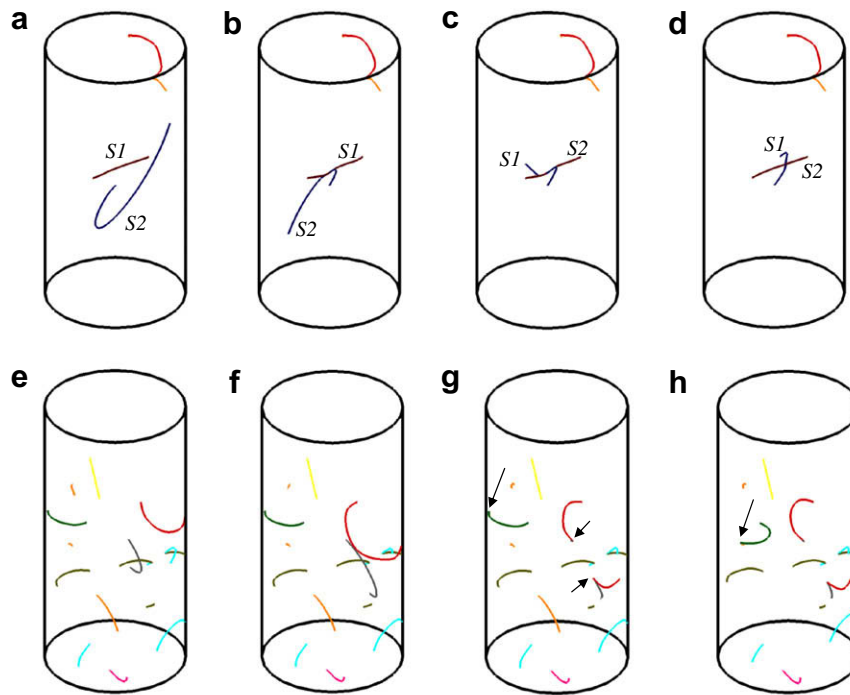


Fig. 9. Dislocation reactions causing flow intermittence: (a–d) glissile junction, brown line with $1/2[\bar{1}01](111)$ and blue line with $1/2[\bar{1}01](1\bar{1}1)$; (e–h) collinear reaction, grey line with $1/2[01\bar{1}](\bar{1}11)$ and red line with $1/2[01\bar{1}](111)$.

was much stronger and could not be easily dissolved, so the new dislocation source was activated in Fig. 9h after the loading increased.

In Ref. [59], strain bursts are attributed to the destruction of jammed configurations by long-range interactions, which produce a collective avalanche-like process. This mechanism seems to be at least somewhat consistent with our observations, as shown in movie A and Fig. 9. The destruction of simple junctions leads to relatively small strain bursts as the released free dislocations quickly escape to the surface. However, the spiral sources released from the junction in Fig. 9 continuously sweep in the slip plane and produce large strain bursts. These strain bursts, or avalanche-like processes, are strongly influenced by their physical size. As illustrated in movie B, the dynamic sources continuously create plastic strain under loading, with the amount of this strain dependent on their position and the sample diameter. From a statistical perspective, the probability of sources truncated by a surface increases with decreasing diameter. Thus the frequency of strain bursts and consequent flow intermittency in smaller samples is much higher than in larger samples, which is verified in both experiment and our simulation results. After the operation of dynamic sources is terminated by a surface, new sources need to be activated at a higher load level to generate continuous plastic deformation. Recently, Ng et al. demonstrated that discrete strain bursts were directly related to the escape of dislocation sources to the sample surface [60], agreeing well with our simulation results and providing a physical explanation of the experimentally observed staircase stress–strain behavior.

3.4. Size effects

In Fig. 10a, we show a series of stress–strain curves from samples with different diameters under uniaxial compression in the absence of loading gradients. These results show pronounced dependence on size, with smaller samples having higher strength. The stress shows discrete jumps accompanied by strain bursts of varying sizes before ending at a saturation flow stress. There is a significant scatter in the magnitude of the saturation flow stress with decreasing diameter. All of these features of the compression stress–strain curves are in qualitative agreement with the experimentally observed behavior that shows discrete strain bursts separated by intervals of nearly elastic loading [2–13].

In Fig. 10b, the variation of the shear stress at 1% strain (τ) as a function of the sample diameter (D) are plotted on a logarithmic scale in both coordinates, for all simulations. The scatter in strength increases with decreasing sample size, largely because the mechanical response of smaller samples depends on a single or, at most very few, active sources. We fit the average value of τ for each size to a function of the form $\tau \propto D^{-n}$ and find a scaling exponent $n \approx 0.67$. Similar behavior in both the magnitude and scatter of the values for the shear stress at 1% strain was seen experimentally, with an exponent of 0.64 under [2 6 9] single-slip loading from Ref. [3] and 0.69 under [1 1 1] multi-slip loading from Ref. [13].

In bulk samples, Taylor's hardening law, which states that the flow stress is proportional to the square root of the dislocation density, has been confirmed by both theo-

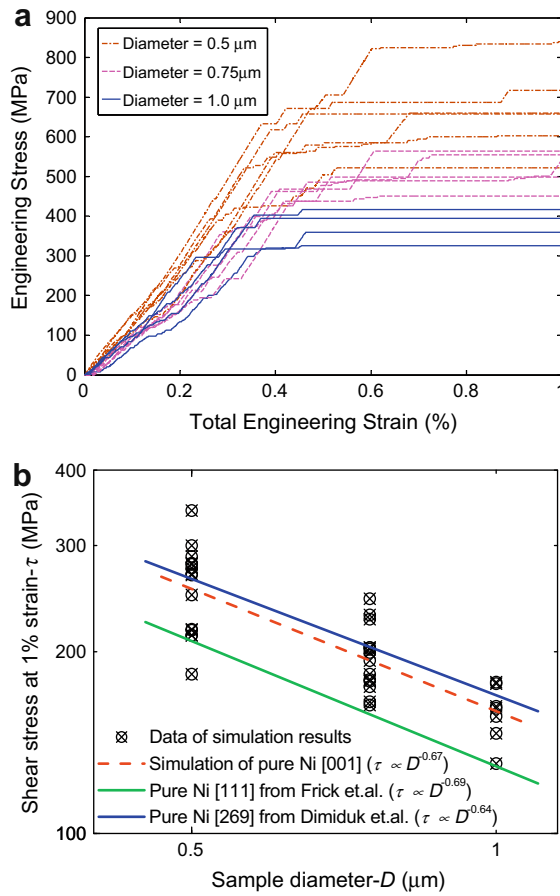


Fig. 10. (a) Stress–strain curves obtained from simulation with different sizes; (b) comparison log–log plot of the shear stress at 1% total strain of simulation results and experimental results.

retical and experimental studies [61]. However, there is little size dependence of the evolution of the dislocation density, since all samples showing similar dislocation density variations as shown in Fig. 6. Thus, Taylor's law does not hold and cannot be used to develop a theory of the size effects of plasticity in small volumes.

Recently, Parthasarathy et al. [62] developed a statistical model for the flow strength of small samples, which was completely based on the stochastics of spiral source (single-arm source) lengths in samples of finite size. In their studies, the spiral source with one permanent inside pinning point could be formed either by the FR sources being truncated at the free surface or directly generated in the initial structure of simulation. In either case, the spiral sources have a minimum strength based on the relative distance between the sources and the free surfaces. For the FR sources, the minimum always appears when the FR source is set at the center of the sample and with the length of around 1/3 the slip-plane characteristic dimension [63]. For a single-arm source, the minimum is set with the source pinning point at the center of the sample [62]. This stochastic model was validated by the in situ observation of dislocation behavior in a sub-micron single crystal in which single-ended sources are limited approximately by half of the crystal width [64].

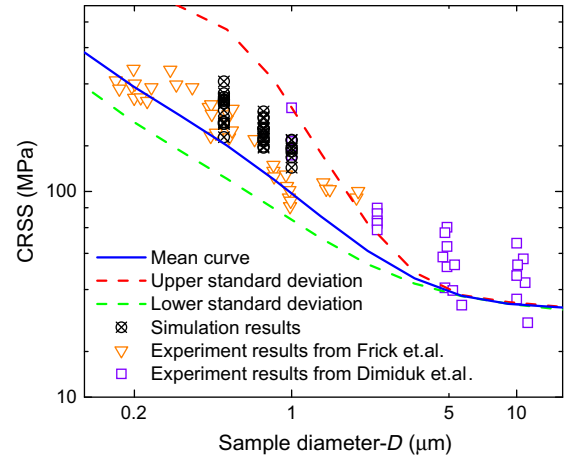


Fig. 11. Comparison log–log plot of the statistic model and simulation and experimental results.

Since the flow stress was always determined by the strength of spiral sources or stable dynamic sources in our simulations, we used our simulation results and experiment results from Refs. [3,13] to compare with this stochastic model, which estimates the critical resolved shear stress (CRSS) as following:

$$\tau = \tau_o + k_s \mu \frac{\ln(\bar{\lambda}/b)}{(\bar{\lambda}/b)} + k_f \mu b \sqrt{\rho_f} \ln \left(\frac{1}{b \sqrt{\rho_f}} \right), \quad (5)$$

where τ_o is the lattice friction stress (11 MPa for Ni), k_s is a source-hardening constant, with magnitude $k_s = 0.12$, derived through a recent study [44], k_f represents the hardening coefficient using a value of $k_f = 0.061$ [65], ρ_f is forest dislocations density, $\rho_f = 2 \times 10^{12} \text{ m}^{-2}$ and $\bar{\lambda}$ is an average effective source length calculated from the statistic model [62]. The second and third term in Eq. (5) represent source truncation strengthening [56] and forest strengthening, respectively. It can be seen from Fig. 11 that this single-arm model could predict the initial stress for plasticity well for smaller samples, because only one or at most a few mobile dislocations determine the strength at small volumes, agreeing with the basic assumption in this model. For the larger samples, the predicted scatter is less than that observed, since internal dislocation structures and reactions are more complicated in larger samples than those in smaller ones.

4. Concluding remarks

Experimental-like initial dislocation structures cut from larger deformed samples have been introduced into 3D DD simulation to study plasticity at small sizes. Image forces from traction-free surface and as well as thermally activated cross-slip were considered in our study. Three different sizes of micropillars, all with initially relaxed dislocation densities around $2.0 \times 10^{13} \text{ m}^{-2}$, have been analyzed under uniaxial compression to identify the relationship between the evolution of internal dislocation structure and overall mechanical behavior.

The results indicate that the loading direction has negligible effect on the flow stress with both multi-slip and single-slip loading, resulting in the similar saturation. This lack of a dependence on loading direction can be easily understood. Since the number of dislocation sources decreases with the sample diameters, the probability of activating a source with low Schmid factors increases in small samples.

In small samples, dynamic sources can be easily generated by cross-slip or collinear reactions, the stability of which depends on the position and sample size. There were at least two origins of “exhaustion hardening”: the escape of dynamic sources from the surface and dislocation interactions such as junction formation. Both of these effects shut off the activated sources, leading to the flow intermittency. The “mechanical annealing” at the early stage of deformation was seen to arise from the surface dislocations and from weakly entangled dislocations leaving the sample. The drop in dislocation density was followed by an increase that always resulted from processes that were enabled by cross-slip. The scarcity of available dislocation sources is a major contribution to the higher flow stress and larger scatter of strength in smaller sizes. The scaling law determined from the current simulation results is close to that found experimentally.

There are still many unanswered questions regarding size-dependent strengthening in small volumes, such as the critical size for transition from bulk behavior and the role that dislocation structures and mechanisms play in determining that critical size. Further investigations are planned for larger samples based on our simulation framework to address these questions. Our goal is to develop a more sophisticated model to predict the mechanical behavior of microcrystals over a wide range of sizes.

Acknowledgements

The authors want to acknowledge many helpful discussions with Dr. Dennis Dimiduk of the Air Force Research Laboratory. This work was supported by the US Department of Energy, Office of Basic Energy Sciences, Division of Materials Sciences and Engineering.

Appendix A. Supplementary material

Supplementary data associated with this article can be found, in the online version, at [doi:10.1016/j.actamat.2009.11.001](https://doi.org/10.1016/j.actamat.2009.11.001).

References

- [1] Herring C, Galt JK. *Phys Rev* 1952;85:1060.
- [2] Uchic MD, Dimiduk DM, Florando JN, Nix WD. *Science* 2004;305:986.
- [3] Dimiduk DM, Uchic MD, Parthasarathy TA. *Acta Mater* 2005;53:4065.
- [4] Dimiduk DM, Uchic MD, Rao SI, Woodward C, Parthasarathy TA. *Model Simul Mater Eng* 2007;15:135.
- [5] Dimiduk DM, Woodward C, LeSar R, Uchic MD. *Science* 2006;312:1188.
- [6] Uchic MD, Shade PA, Dimiduk DM. *Annu Rev Mater Res* 2009;39:361.
- [7] Greer JR, Nix WD. *Appl Phys A* 2005;80:1625.
- [8] Greer JR, Nix WD. *Phys Rev B* 2006;73:245410.
- [9] Greer JR, Oliver WC, Nix WD. *Acta Mater* 2005;53:1821.
- [10] Ng KS, Ngan AHW. *Philos Mag Lett* 2007;87:967.
- [11] Brinckmann S, Kim JY, Greer JR. *Phys Rev Lett* 2008;100:15502.
- [12] Volker CA, Lilleodden ET. *Philos Mag* 2006;86:5567.
- [13] Frick CP, Clark BG, Orso S, Schneider AS, Artz E. *Mater Sci Eng A* 2008;489:319.
- [14] Wu B, Heidelberg A, Boland JJ. *Nat Mater* 2005;4:525.
- [15] Espinosa HD, Prorok BC, Fischer M. *J Mech Phys Solids* 2004;52:667.
- [16] Bei H, Shim S, Pharr GM, George EP. *Acta Mater* 2008;56:4762.
- [17] Ng KS, Ngan AHW. *Acta Mater* 2008;56:1712.
- [18] Shan ZW, Mishra RK, Asif SAS, Warren OL, Minor AM. *Nat Mater* 2008;7:115–9.
- [19] Budiman AS, Han SM, Greer JR, Tamura N, Patel JR, Nix WD. *Acta Mater* 2008;56:602.
- [20] Maass R, Grolimund D, van Petegem S, et al. *Appl Phys Lett* 2006;89:151905.
- [21] Maass R, Van Petegem S, Zimmermann J, Borca CN, Van Swygenhoven H. *Scripta Mater* 2008;59:471.
- [22] Robertson IM, Ferreira PJ, Dehm G, Hull R, Stach EA. *MRS Bull* 2008;33:122.
- [23] Hague MA, Saif MTA. *Proc Nat Acad Sci* 2004;101:6335.
- [24] Minor AM, Asif SAS, Shan ZW, Stach EA, Cyranowski E, Wyrobek T, Girshick SL. *Nat Mater* 2006;5:697.
- [25] Liu WK, Karpov EG, Zhang S, Park HS. *Comput Methods Appl Mech Eng* 2004;193:1529.
- [26] Gulluoglu AN, Srolovitz DJ, LeSar R, Lomdahl PS. *Scripta Metall* 1989;23:1347.
- [27] Ghoniem NM, H Tong S, Sun LZ. *Phys Rev B* 2000;61:913.
- [28] Kubin LP, Canova G. *Scripta Metall Mater* 1992;27:957.
- [29] Zbib HM, de la Rubia TD, Rhee M, Hirth JP. *J Nucl Mater* 2000;276:154.
- [30] Devincere B, Kubin LP, Hoc T. *Scripta Mater* 2006;54:741.
- [31] Deshpande VS, Needleman A, van der Giessen E. *J Mech Phys Solids* 2005;53:2661.
- [32] Deshpande VS, Needleman A, van der Giessen E. *Mater Sci Eng A* 2005;400–401:154.
- [33] Guruprasad PJ, Benzerga AA. *J Mech Phys Solids* 2008;56:132.
- [34] Tang H, Schwarz KW, Espinosa HD. *Acta Mater* 2007;55:1607.
- [35] Rao SI, Dimiduk DM, Parthasarathy TA, Uchic MD, Tang M, Woodward C. *Acta Mater* 2008;56:2988.
- [36] Weygand D, Pognant M, Gumbsch P, Kraft O. *Mater Sci Eng A* 2008;483:188.
- [37] Senger J, Weygand D, Gumbsch P, Kraft O. *Scripta Mater* 2008;58:587.
- [38] El-Awady J, Biner SB, Ghoniem NM. *J Mech Phys Solids* 2008;56:2019.
- [39] Tang H, Schwarz KW, Espinosa HD. *Phys Rev Lett* 2008;100:185503.
- [40] Motz C, Weygand D, Senger J, Gumbsch P. *Acta Mater* 2009;57:1744.
- [41] van der Giessen E, Needleman A. *Model Simul Mater Eng* 1995;3:689.
- [42] El-Awady J, Wen M, Ghoniem NM. *J Mech Phys Solids* 2009;57:32.
- [43] Hirth JP, Lothe J. *Theory of dislocations*. 2nd ed. New York: Wiley-Interscience; 1982.
- [44] Puschl W. *Prog Mater Sci* 2002;47:415.
- [45] Verdier M, Fivel M, Canova I. *Model Simul Mater Eng* 1998;6:755.
- [46] Friedel J. In: Fisher J, Johnston W, Thomson R, Vreeland T, editors. *Dislocations and mechanical properties of crystals*. New York: Wiley-Interscience; 1957.

- [47] Escaig B. In: Rosenfield A, Hahn G, Bement A, Jaffee R, editors. *Proceedings of the Battelle colloquium in dislocation dynamics*. New York: McGraw-Hill; 1968.
- [48] Rao S, Parthasarathy T, Woodward C. *Philos Mag A* 1999;79:1167.
- [49] Starenchenko V, Lychagin D, Shaekhov R, Kozlov A. *Russ Phys J* 1999;42:653.
- [50] Wang ZQ, Beyerlein IJ, LeSar R. *Model Simul Mater Eng* 2007;15:675.
- [51] Wang ZQ, Beyerlein IJ, LeSar R. *Int J Plast* 2009;25:26.
- [52] Norfleet DM, Dimiduk DM, Polasik SJ, Uchic MD, Mills MJ. *Acta Mater* 2008;56:2988.
- [53] Ng KS, Ngan AHW. *Scripta Mater* 2008;58:796.
- [54] Weinberger CR, Cai W. *PNAS* 2008;105:14304.
- [55] Shim S, Bei H, Miller MK, Pharr GM, George EP. *Acta Mater* 2009;57:503.
- [56] Rao SI, Dimiduk DM, Tang M, Parthasarathy TA, Uchic MD, Woodward C. *Philos Mag* 2007;87:4777.
- [57] Madec R, Devincere B, Kubin LP, Hoc T, Rodney D. *Science* 2003;301:1879.
- [58] Gilman JJ, Johnston WG. *Solid State Phys* 1962;13:147.
- [59] Csikor FF, Motz C, Weygand D, Michael Z, Zapperi S. *Science* 2007;318:251.
- [60] Ng KS, Ngan AHW. *Acta Mater* 2009;57:4902.
- [61] Kocks UF, Mecking H. *Physics and phenomenology of strain hardening: the FCC case*. *Prog Mater Sci* 2003;48:171.
- [62] Parthasarathy TA, Rao SI, Dimiduk DM, Uchic MD, Trinkle DR. *Scripta Mater* 2007;56:313.
- [63] Blankenhagen BV, Gumbsch P, Arzt E. *Philos Mag Lett* 2003;83:1.
- [64] Oh SH, Legros M, Kiener D, Dehm G. *Nat Mater* 2009;8:95.
- [65] Basinski ZS. *Scripta Metall* 1974;8:1301.